

Next Generation Very Large Array Memo No. 61

Temporal and Spatial Tropospheric Phase Fluctuations at the VLA (and Beyond) and Implications for Phase Calibration

Christopher A. Hales (NRAO Socorro)

March 15, 2019; updated December 5, 2019* and March 31, 2020†

Abstract

I examine temporal and spatial root phase structure functions arising from tropospheric water vapor over the VLA using observations of two calibrators in large array configurations, the first observed in winter at night time (good atmospheric conditions) and the second observed in summer in the late afternoon (poor atmospheric conditions). I infer a general equation that predicts the growth of rms phase fluctuations on a baseline over time, with focus on small timescales associated with measurements in the regime of 3-dimensional (thick screen) turbulence. This equation has power-slope 0.8 (closely matching theory) and upper-limit intercept $0.6^\circ/\text{GHz}$ at 10 sec, and is independent of baseline length, time of day, time of year, and likely even geographic location. While the intercept will be a factor few lower under optimal observing conditions (down to an order of magnitude lower at exceptional high dry sites like the Chajnantor plateau), the upper-limit relationship presented here is relevant for considering performance of large arrays over which subsets of antennas may be concurrently experiencing different atmospheric conditions. I use the rms phase growth relationship to derive an equation relating phase calibration timescale and image dynamic range limit. Using this relationship, I assess several phase calibration strategies for their capacity to support an image dynamic range requirement, demonstrating calculations relevant to the ngVLA.

1 Introduction

The propagation of radio waves through the neutral atmosphere gives rise to interferometric phase fluctuations that are predominantly caused by temporal variations in tropospheric water vapor content (dry atmospheric gases also contribute, as do ice particles when present). Changes in the index of refraction due to the wet component are essentially non-dispersive at frequencies relevant to the ngVLA below 120 GHz, with only small ($< 1\%$) dispersive contributions associated with resonances. As a result, tropospheric phase variations scale linearly with frequency.

*Calculations after Equation 6 updated to satisfy revised ngVLA 45 dB dynamic range requirement.

†Revised discussion from Equation 5 onwards.

Phase calibration seeks to track variations in tropospheric phase to within acceptable rms limits. By performing phase calibration on ever faster timescales, residual phase errors can be minimized, yielding smaller visibility measurement errors and raising image dynamic range limits (Hales 2019). But how quickly do rms phase errors ‘build up’ over time as a function of baseline length and atmospheric conditions? What are the scaling relationships? This is important to understand for ngVLA design, where technical requirements need to be defined in part by the need to support high dynamic range imaging for deep field science.

The answer to this question can be obtained by turning to the theory of Kolmogorov turbulence, which is well established for describing atmospheric phase fluctuations (Thompson, Moran & Swenson 2017, chapter 13 and references therein). Qualitatively, as a function of increasing observing time, rms phase fluctuations on a given baseline are at first expected to rise with steep power-law slope, followed by a shallower slope, before ultimately flattening at a ‘saturation’ rms phase. Short baselines are expected to only exhibit the initial steep slope prior to saturating. This short baseline behavior has been seen with atmospheric phase monitors around the world, which typically operate by observing a geostationary satellite beacon over a ~ 300 m baseline (e.g. Holdaway et al. 1995; Butler & Desai 1999). However, I have been unable to locate an empirical demonstration on longer baselines where the initial steep power-law slope can be verified and where all three slopes should be observable.

In this memo I examine VLA observations of two bright calibrators, the first observed in winter at night time (best-case atmospheric conditions), and the second observed in summer in the late afternoon (worst-case atmospheric conditions, though short of observing in a thunderstorm). I construct spatial and temporal root structure functions and use these data to draw general conclusions about the temporal behavior of tropospheric phase fluctuations as functions of baseline length and observing conditions. I then demonstrate how this information can be used to satisfy a minimum dynamic range constraint with relevance for ngVLA design.

2 Theory of Tropospheric Phase Fluctuations

When an interferometer observes an unresolved source, the difference in observed phase ϕ between two antennas separated by baseline length d is $[\phi(x) - \phi(x + d)]$. Phase differences will arise from fluctuations in the refractive index of the troposphere. These fluctuations are typically described by a Kolmogorov spectrum, where the spatial root phase structure function (rms phase fluctuations vs baseline length) is a power law of form

$$D_{\phi}^{0.5}(d) = \sqrt{\langle [\phi(x) - \phi(x + d)]^2 \rangle} \propto d^{\beta}. \quad (1)$$

For given length scale d , the structure function is insensitive to atmospheric fluctuations on longer scales. Phase fluctuations can also be described by the temporal root phase structure function,

$$D_{\phi}^{0.5}(\tau) = \sqrt{\langle [\phi(t) - \phi(t + \tau)]^2 \rangle} \propto \tau^{\beta}, \quad (2)$$

which characterizes rms phase fluctuations as a function of time lag τ on baseline length d . Under the ‘frozen screen’ hypothesis, turbulent eddies are assumed to remain fixed as the atmospheric layer advects over the array at characteristic velocity aloft v_a . Under this

approximation, baseline length and time are related such that $D_\phi(\tau) = D_\phi(d = v_a\tau)$. A practical implication to ensure robust statistical sampling of a temporal or spatial structure function is that an observation timespan must be much longer than the baseline crossing time d/v_a , or alternatively it must sample an ensemble of many baselines of length d . The assumption of frozen screen advection is not appropriate for severe weather like thunderstorms.

The expected theoretical scaling for β is summarized in Table 13.2 from Thompson, Moran & Swenson (2017). Baselines (or timescales) shorter than the thickness of the turbulent layer will be dominated by 3-dimensional turbulence (thick screen) with $\beta = 5/6$, longer baselines will be dominated by 2-dimensional turbulence (thin screen) with $\beta = 1/3$, and baselines exceeding the outer length scale of the turbulence will saturate with $\beta = 0$.

3 Data

I obtained archival VLA observations of the compact calibrators 0748+240 and 3C273. Each were observed for an extended time period in a large array configuration, and selected here to respectively sample calm atmospheric conditions at night time in winter and more active conditions in the late afternoon in summer.

0748+240 was observed with the VLA in BnA configuration on January 29, 1997 between 04:43–06:07 UTC (local time 21:43–23:07 MST), yielding 84 min continuous observing time on source. The integration time was 10 sec. This is the same dataset that was used to calculate the spatial root phase structure function presented in Figure 1 from Carilli & Holdaway (1997). Baseline phases from the *RR* polarization product from one of the spectral windows at observing frequency 22.4851 GHz were selected. The mean phase for each baseline’s unwrapped phase time series was subtracted in preparation for computing the structure functions. To enable comparison with the 3C273 data described below, this procedure was also performed using only the first 25 min of data from the full 84 min observation.

3C273 was observed with the EVLA in A configuration on August 5, 2015 between 23:40–24:05 UTC (local time 17:40–18:05 MDT), yielding 25 min continuous observing time on source. The integration time was 1 sec. The observing logs prior to and after the observation indicate mixed clouds, falling from 80% to 30% sky coverage throughout the observation. No thunderstorms were noted. The data were calibrated for time-independent delay and bandpass. For each integration on each baseline, the *RR* visibilities from all channels within one of the spectral windows centered at observing frequency 33.943 GHz were averaged together to yield a phase time series per baseline. As above, the mean phase for each baseline’s unwrapped phase time series was then subtracted in preparation for computing the structure functions.

Spatial and temporal root structure functions were then calculated. These are presented in the following section. To enable quantitative comparison between the results from 0748+240 and 3C273, the phases in all figures presented in this work have been scaled in units of deg/GHz (i.e. phases were divided by their respective observing frequencies). This also simplifies the prediction of phase fluctuations at other observing bands (simply multiply by the frequency in GHz, though note that this memo does not consider ionospheric phase contributions).

To aid comparison between the winter and summer data, hourly and seasonal variations in median rms phase measured on a 300 m baseline by the atmospheric phase monitor at the

VLA site, from Butler (2019), are shown in Figure 1. These data and other monitor statistics are examined in more detail by Butler (2019).

4 Results

To illustrate the data quality and enable comparison between the input data and output structure functions, the phase time series for three representative baselines in each dataset (length in 3D range, 2D range, and beyond outer scale) are displayed in Figure 2. These baselines are identified visually in the structure function plots described below.

The spatial root phase structure functions seen toward 0748+240 using the 84 min and 25 min datasets are presented in Figure 3. The filled circles in the right panels were calculated by subtracting in quadrature a constant instrumental noise term of $0.5^\circ/\text{GHz}$ following Carilli, Holdaway & Ishiguro (1996). The fit in the right panels is from Carilli & Holdaway (1997). This fit is divided into three regions that correspond to thick screen (3D) turbulence at $d < 1.2$ km with $\beta_{\text{fit}} = 0.85$, thin screen (2D) turbulence at $1.2 < d < 6$ km with $\beta_{\text{fit}} = 0.41$, and an outer scale of turbulence at $d > 6$ km with $\beta_{\text{fit}} = 0.1$. The spatial root phase structure function seen toward 3C273 is presented in Figure 4. The corresponding temporal root phase structure functions seen toward 0748+240 and 3C273 are presented in Figures 5 and 6, respectively.

The 84 min spatial structure function seen toward 0748+240, displayed in the upper panels in Figure 3, exhibits a steep power-law rise on short baselines that flattens at 1.2 km and flattens further beyond 6 km. The corresponding temporal structure function in Figure 5 exhibits a similar break from the steepest initial slope to a flattened yet still rising slope at 120 sec. This is followed by flattening to a constant rms phase that matches the value found in the spatial structure function; to illustrate, compare the saturation rms phases for the baselines displayed in the top left panel in Figure 5 with the corresponding highlighted values in the top left panel in Figure 3. Using the frozen screen approximation, the 1.2 km and 120 sec boundaries for thick screen turbulence indicate typical wind speeds aloft $v_a \approx 10$ m/s. This speed is consistent with typical values reported elsewhere for the VLA and other facilities worldwide.

For wind speed 10 m/s and baseline length 6 km, there are only 2.5 independent tropospheric crossing times within a 25 min observing period. This is insufficient for robust statistical sampling. As a result, the spatial and temporal structure functions constructed using the 25 min dataset for 0748+240, and for 3C273, exhibit steeper slopes than expected theoretically for thin screen turbulence. The turnover on long baselines, seen most dramatically in the lower right panel of Figure 3, is also due to this limitation, where the crossing time for a 20 km baseline is 33 min. The spatial structure function seen toward 3C273 likely exhibits a rise on the longest baselines that is erased and flattened by a turnover from limited statistical sampling. Additionally, it is likely that limited statistical sampling is responsible for the steeper than expected slopes observed beyond a few km in the 84 min 0748+240 data, where only 12 crossing times are sampled on 4 km baselines, and only 2.5 crossing times are sampled on 20 km baselines. The spatial structure functions and their observed boundaries and slopes are therefore in good agreement with the Kolmogorov expectations for tropospheric

wet¹ turbulence. The ratio between saturation phases observed in summer and winter on a 500 m baseline (the shortest available for 3C273, and also the least likely to be affected by statistical sampling bias) is approximately 6. This is consistent with the ratio of 5 predicted using the median weather statistics presented in Figure 1.

Despite the much larger saturation rms phases observed in the spatial structure function seen toward 3C273 versus 0748+240, the temporal structure functions in Figures 5 and 6 exhibit similar magnitude behavior at small time lags. They each exhibit an initial steep rise followed by shallower rise, with slopes well matched to the values expected from theory. The 25 min data for 0748+240 and 3C273 exhibit a consistent thin screen slope of 0.42, slightly steeper than theory. Given that these data reflect significantly different atmospheric conditions (best-case winter vs worst-case summer), this suggests that the steepened slope may simply reflect insufficient statistical sampling on the longest timescales. Indeed, this would be consistent with the arguments presented above. Importantly, of interest for the discussion in the following section, the thick screen regions at small time lags in the temporal structure functions appear to be unaffected by observing epoch (time of day or seasonal effects).

5 Discussion

The behavior of the temporal root phase structure functions in the thick screen region at small time lags can be conservatively approximated by a power law with slope 0.8 and 10 sec intercept at $K = 0.6^\circ/\text{GHz}$. The motivation for this intercept is as follows. The intercept in the VLA winter data is $0.2^\circ/\text{GHz}$ while in the summer data it is $0.4^\circ/\text{GHz}$. This ratio of 2 is less than the factor of 6 identified in the previous section for saturation phases on 500 m baselines or anticipated from Figure 1. The scaling of rms phase fluctuations on short timescales is therefore not as dramatic as exhibited by saturation rms values. Assuming that the factor of 2 is approximately valid for scaling to even worse atmospheric conditions, then a factor of 9 in rms saturation values above the VLA winter conditions would yield an intercept at $0.6^\circ/\text{GHz}$. To place this in context, a factor 7.5 in Figure 1 is the difference between night time in winter and the peak rms phase fluctuations seen in summer at 20 UTC. Alternatively, if comparing the mean water vapor content over the high desert plains at the VLA site against the US eastern seaboard, or indeed against any location worldwide, then this ratio is less than 5. For example, see the global water vapor maps at <https://www.earthobservatory.nasa.gov/global-maps> or the ten year average global map presented in Figure 13.2 from Thompson, Moran & Swenson (2017). This ratio of 5 effectively includes the scaling of rms phase fluctuations with site altitude, for example presented in Figure 13.18 from Thompson, Moran & Swenson (2017). Thus the value of K selected above should be suitable for all proposed baselines of the ngVLA, or any radio observatory site worldwide. Modeling with slope 0.8 will ensure a slightly shallower decline at $\tau < 10$ sec versus theory (0.83) while not significantly underestimating rms phase fluctuations on longer timescales (this is also mitigated by a conservatively high intercept). For comparison, optimal observing conditions at the ALMA site exhibit a 10 sec intercept at $0.03^\circ/\text{GHz}$ (Holdaway et al. 1995). This is an order of magnitude lower than at the VLA site and approximately consistent with the scaling argument above.

¹Water vapor is poorly mixed in the atmosphere, so turbulence identified in the wet phase will only represent a portion of the total energetics associated with atmospheric turbulence.

The temporal results can therefore be summarized into a single equation for baseline rms phase fluctuations arising from tropospheric wet turbulence,

$$D_{\phi}^{0.5}(\tau) < 0.6 \nu \left(\frac{\tau}{10} \right)^{0.8} \text{ deg} , \quad (3)$$

for observing frequency ν in GHz and time lag τ in seconds. This equation is independent of baseline length, time of day, time of year, and geographic location. Note that antenna-based rms phase fluctuations are a factor $\sqrt{2}$ smaller than given by Equation 3 because baseline phase is the difference between two antenna phases. Note also that Equation 3 does not account for the saturation rms phase level, which could be small for very short baselines. Equation 3 is only valid for timescales out to the baseline length or the turbulent layer thickness ~ 1 km, whichever is less, where the latter is ~ 100 sec for $v_a = 10$ m/s. For longer timescales, the thin screen slope or saturation level must be connected. For the purpose of the following discussion, Equation 3 is sufficient for estimating typical visibility measurement errors resulting from phase calibration timescales less than 30 sec for an array with baselines spanning sub-km to continental-scales.

Rearranging and modifying Equation 3, the maximum timescale t_{Φ} over which antenna-based rms phase fluctuations will remain below a threshold Φ is given by

$$t_{\Phi} < 29 \left(\frac{\Phi}{\nu} \right)^{1.25} \text{ sec} , \quad (4)$$

where Φ is in degrees and ν is in GHz, and with the same caveats as above.

Similarly, Equation 3 can be combined with Equations 9 and 10 from Hales (2019) to estimate the maximum timescale for phase calibration t_{pcal} that is required to satisfy a dynamic range limit D for an image of a Stokes parameter (e.g. Stokes I) when observing for M statistically independent timescales with an array comprising N dual-polarization receivers. The result is

$$t_{pcal} < 1900 \frac{N^{1.25} M^{0.625}}{(\nu D)^{1.25}} \text{ sec} , \quad (5)$$

or rearranged to calculate dynamic range

$$D \approx 430 \frac{N \sqrt{M}}{\nu t_{pcal}^{0.8}} , \quad (6)$$

where t_{pcal} is in seconds.

To demonstrate Equation 6, consider the science-driven requirement for ngVLA to facilitate 45 dB image dynamic range from an observation at 8 GHz spanning a few hours. For this calculation I will assume that the wet troposphere is the only contributor to visibility measurement errors and I will ignore anomalous refraction. There are a few common approaches to phase calibration when operating under demanding conditions.

The first is fast switching phase calibration, in which the antennas repeatedly slew between a science target and nearby calibrator, transferring the atmospheric phase on the calibrator to the science target. The cycle time between cal-tar-cal is limited by mechanical constraints of the antennas, and becomes increasingly impractical on timescales less than 10 sec. On-target

efficiency also becomes very low after accounting for time on calibrator. More fundamentally, when accounting for the typical angular separation (and thus different atmospheric lines of sight) between calibrator and target, the minimum effective baseline or timescale (assuming equivalence using $v_a = 10$ m/s) for fast switching calibration is ~ 100 m or 10 sec (Carilli 2015). This is the best-case timescale on which phase fluctuations can be effectively tracked. Assuming a 3.5 hour observation², the largest phase fluctuations that can limit dynamic range will be sampled on 10 sec timescales, in which case each antenna will effectively sample $M = 1260$ independent timescales. Assuming an array with $N = 107$ antennas (half the Main Array, accounting for potential tapering), Equation 6 predicts that the limiting dynamic range will be 45 dB. Given that this is the best-case dynamic range, with a possible improvement factor of only a few at most (if observations are scheduled to coincide with the winter K value), it will not be possible to satisfy the 45 dB requirement with switching timescales longer than 10 sec. Therefore, a fast switching approach will necessarily impose low observing efficiency for high dynamic range projects (as well as other considerations such as increased antenna wear rates). As a result, fast switching is not an optimal solution for the ngVLA where high on-target observing efficiency is sought (ideally 90%).

A second approach is paired array calibration, in which a subset of antennas view a nearby calibrator while the others view the target. The constraints are set by the baseline length between target and calibration antennas, and are thus the same as with 10 sec fast switching above. While this approach is promising over short baselines, it is not possible for antennas with nearest neighbors separated by more than 100 m. It is also inherently wasteful of array resources, as otherwise capable antennas (even if provided by dedicated small-diameter dishes) are unavailable for observing science targets. Therefore, paired array calibration is in general undesirable for the ngVLA.

A third approach is self-calibration. To achieve 45 dB image dynamic range at 8 GHz, Equation 5 indicates that solutions must be obtained within $0.12M^{0.625}$ sec. For a 3.5 hour observation this is satisfied with a timescale of 10 sec ($M = 1260$). The anticipated continuum sensitivity of the ngVLA at 8 GHz in time interval 10 sec, combining both polarizations (correlated phases), on $N - 1 = 106$ baselines toward a single antenna, and within a (wide) 10% fractional bandwidth (880 MHz) is $\sigma \approx 0.2$ mJy/beam. The antenna-based phase measurement error resulting from observation of an unresolved source with flux density S is given by $\sigma_{\phi_{a,meas}} = \sigma/S$ (e.g. Equation 9.67 from Thompson, Moran & Swenson 2017). The noise in a self-calibration solution cannot be larger than the tropospheric phase noise on lag timescale 10 sec, namely $\sigma_{\phi_{a,meas}} < \Phi$. Using Equation 4 and rearranging, the source flux density must therefore satisfy $S > 3$ mJy. This demonstrates that self-calibration will be suitable for some science objectives. However, it is unlikely to be sufficient for deep field studies (which drive the 45 dB requirement) where fields are typically selected to avoid mJy-level sources (e.g. existing deep fields with the JVLA). If the brightest source suitable for self-calibration in the field is less than 3 mJy, then the tradeoff associated with increased self-calibration integration

²An observation length of 3.5 hours is selected for two reasons. First, this is the approximate timescale over which the anticipated continuum sensitivity of the ngVLA at 8 GHz with $N = 107$ antennas is expected to yield 45 dB image dynamic range for an unresolved source with flux density 7 mJy. And second, as calculated for the self-calibration approach, 3 mJy is the approximate flux density threshold at which the noise from self-calibration solutions will induce phase errors that exceed the threshold necessary to achieve 45 dB dynamic range (i.e. self-calibration will not be possible with unresolved sources fainter than ~ 7 mJy).

time (decreased $\sigma_{\phi_{a,meas}}$, increased Φ) and increased observing time (adjusted M) may lead to unreasonable demands for observing time in which the thermal noise limit will be wastefully below the dynamic range floor. Therefore, self-calibration may not always be sufficient for the ngVLA.

A fourth approach is to perform simultaneous multi-frequency observations (e.g. Dodson et al. 2017). The capability to perform such observations is not part of the current ngVLA reference design, though it is not ruled out for the final design. This is effectively self-calibration, but utilizing an in-beam source (target or nearby) that is brighter at a lower frequency. The calculation above for self-calibration was performed near the most sensitive anticipated portion of ngVLA frequency space. Therefore, the flux density limit above is relevant here, where even stronger sources may be required to offset different continuum sensitivities between frequency bands (though a calibrator with steep spectral index may offset this somewhat). Furthermore, phases observed at frequencies below 8 GHz will be corrupted by the ionosphere and therefore of limited utility in addressing the 45 dB dynamic range requirement. Therefore, while suitable for some science, this technique will not be sufficient for the ngVLA.

Finally, a fifth approach is to employ radiometric phase correction, for example using the 22 GHz water line (Thompson, Moran & Swenson 2017). As above, the timescale for tracking phase fluctuations in order to satisfy a dynamic range limit of 45 dB must be around 10 sec. This sampling timescale is within realistic parameter space for water vapor radiometers (issues regarding the practicality of building such a radiometer with sufficient sensitivity for ngVLA are currently under investigation and are beyond the scope of this memo). Given the limitations identified for the previous calibration techniques, the conclusion is that water vapor radiometry is essential for ngVLA. Comparison with the fast switching technique also implies that, ideally, a radiometer should be placed on every 18 m diameter antenna because the effective length scale associated with 10 sec and $v_a = 10$ m/s is only 100 m. This is close to the shortest anticipated baseline length of 30 m between ngVLA 18 m antennas. A conceivable alternative may be to neglect placing radiometers on antennas located within 100 m of a designated radiometer-equipped antenna, though any cost saving from slightly fewer radiometers may be outweighed by the additional complexity and automation costs of handling a hybrid calibration approach.

References

- Butler B., Desai K., 1999, VLA Test Memo No. 222
 Butler B., 2019, ngVLA Memo, in prep.
 Carilli C. L., Holdaway M. A., Ishiguro M., 1996, VLA Scientific Memo No. 171
 Carilli C. L., Holdaway M. A., 1997, VLA Scientific Memo No. 173
 Carilli C. L., 2015, ngVLA Memo No. 1
 Dodson R., Rioja M. J., Jung T., et al., 2017, *New Astronomical Reviews*, 79, 85
 Hales C. A., 2019, ngVLA Memo No. 60
 Holdaway M. A., Radford S. J. E., Owen F. N., Foster S. M., 1995, ALMA Memo No. 129
 Thompson A. R., Moran J. M., Swenson G. W., 2017, *Interferometry and Synthesis in Radio Astronomy*, 3rd ed., Springer

VLA Site 50th percentile API RMS Phase vs. UTC time of day – 1997–2015

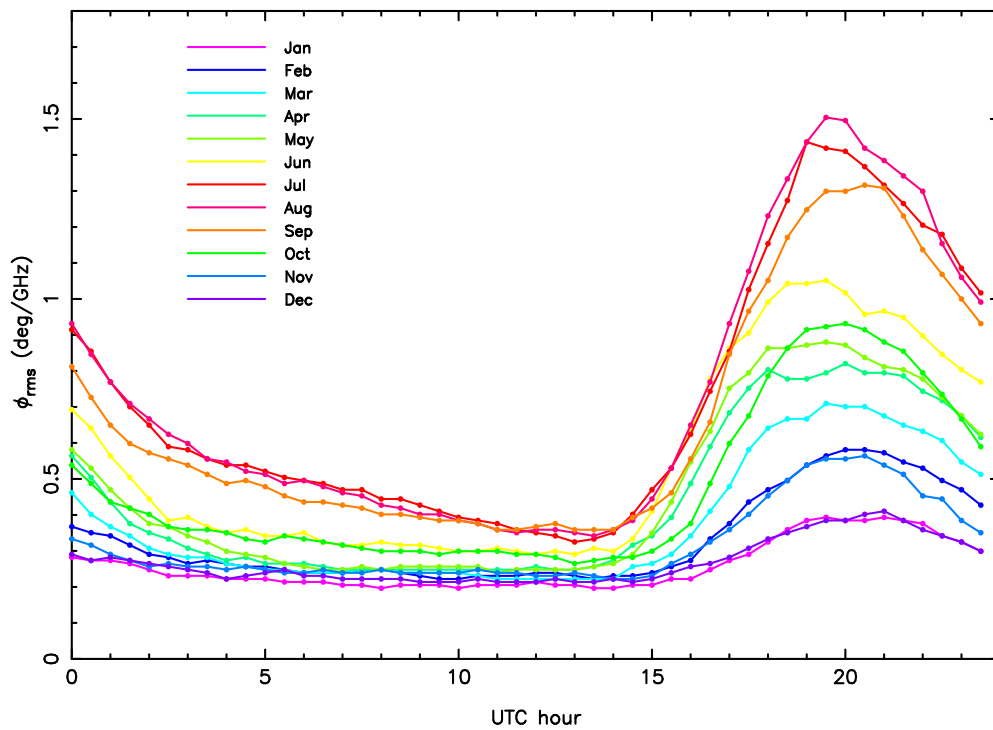


Figure 1 Hourly and seasonal variations in tropospheric median rms phase measured by the atmospheric phase monitor at the VLA (300 m east-west baseline observing a GPS satellite beacon at 11.7 GHz) between 1995 to 2015, adapted from Butler (2019). Measurements were calculated over a 10 min period after subtracting any linear trend. Note that Mountain Standard Time (MST) = UTC – 7h.

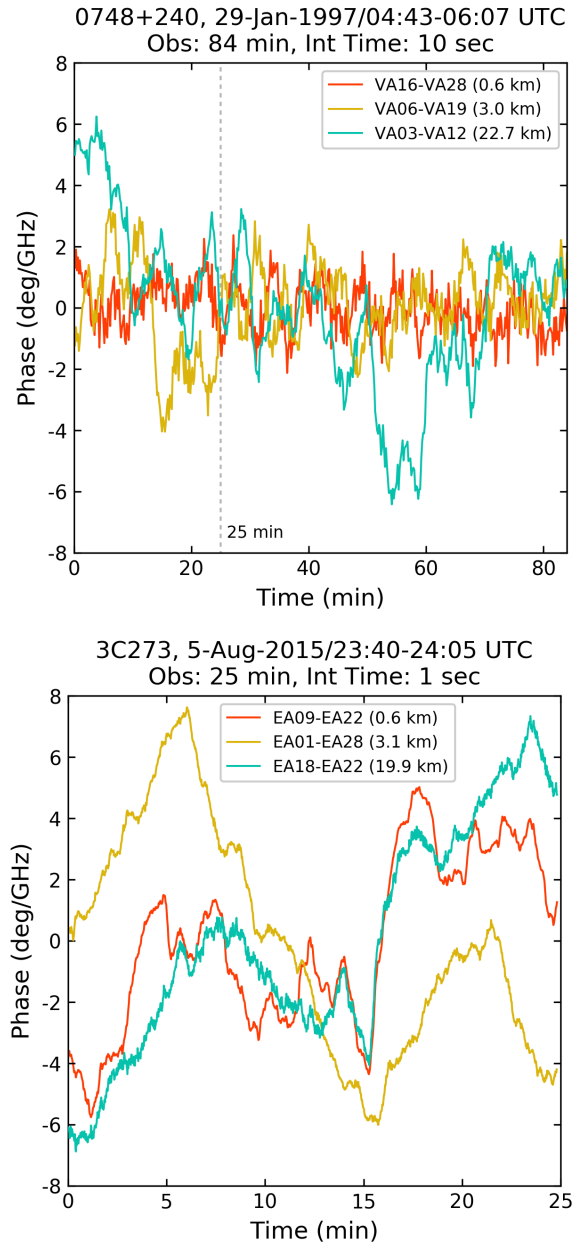


Figure 2 Phase time series for three baselines observing 0748+240 (left) and 3C273 (right). See panel titles and legends for details. Note that the left panel spans 84 min while the right spans 25 min. These baselines are identified in the respective structure functions presented in Figures 3–6.

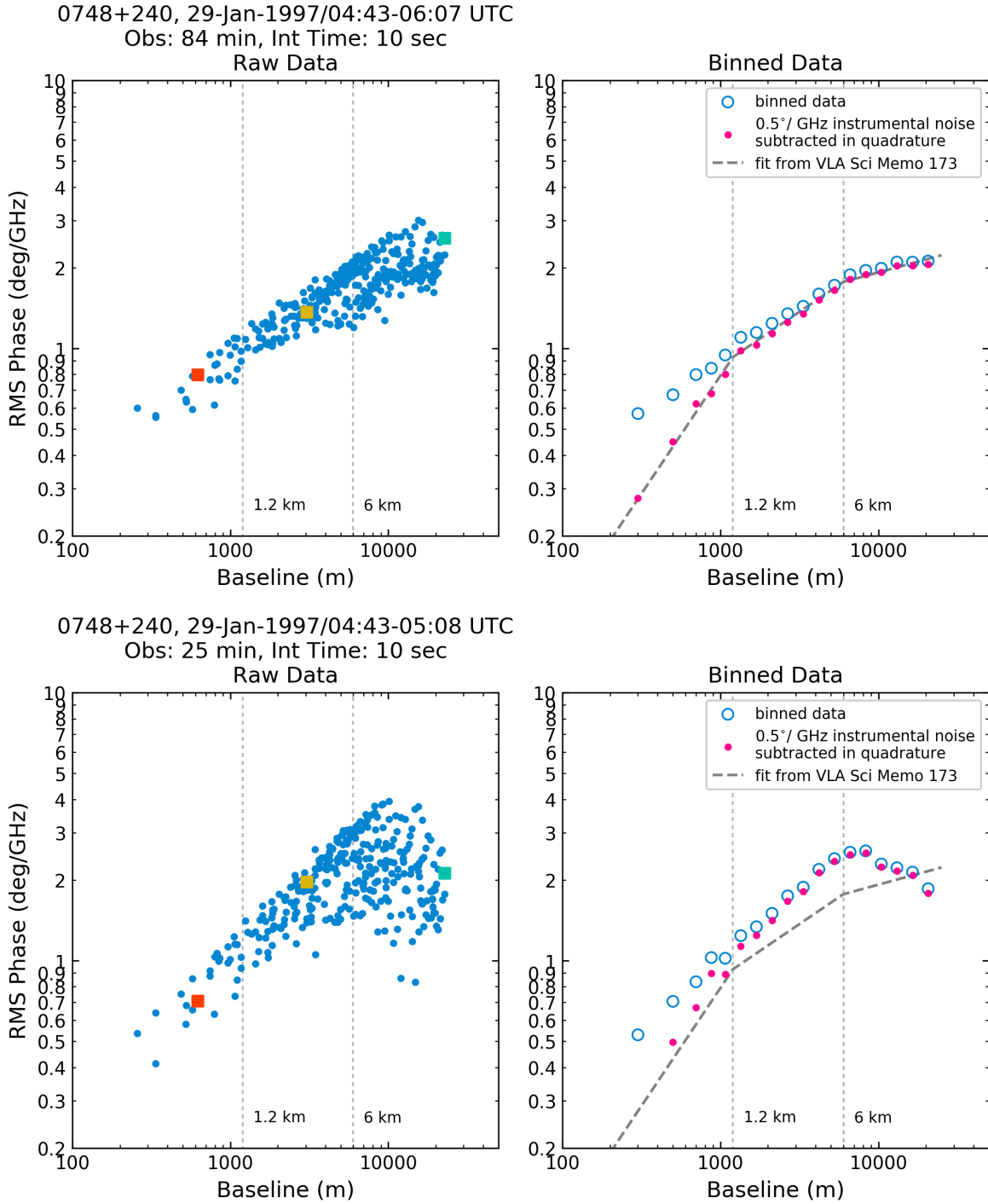


Figure 3 *Upper panels:* Spatial root phase structure function from an 84 min observation of 0748+240 with the VLA in BnA configuration starting at 9:43 pm local time on January 29, 1997. The left panel displays rms phase variations versus baseline length for all baselines. The right panel shows binned values. The fit in the right panel is from Carilli & Holdaway (1997) with boundaries indicating the transitions between 3D, 2D, and the outer scale of turbulence. *Lower panels:* Same as upper panels but calculated using data from only the first 25 min of the full 84 min observation.

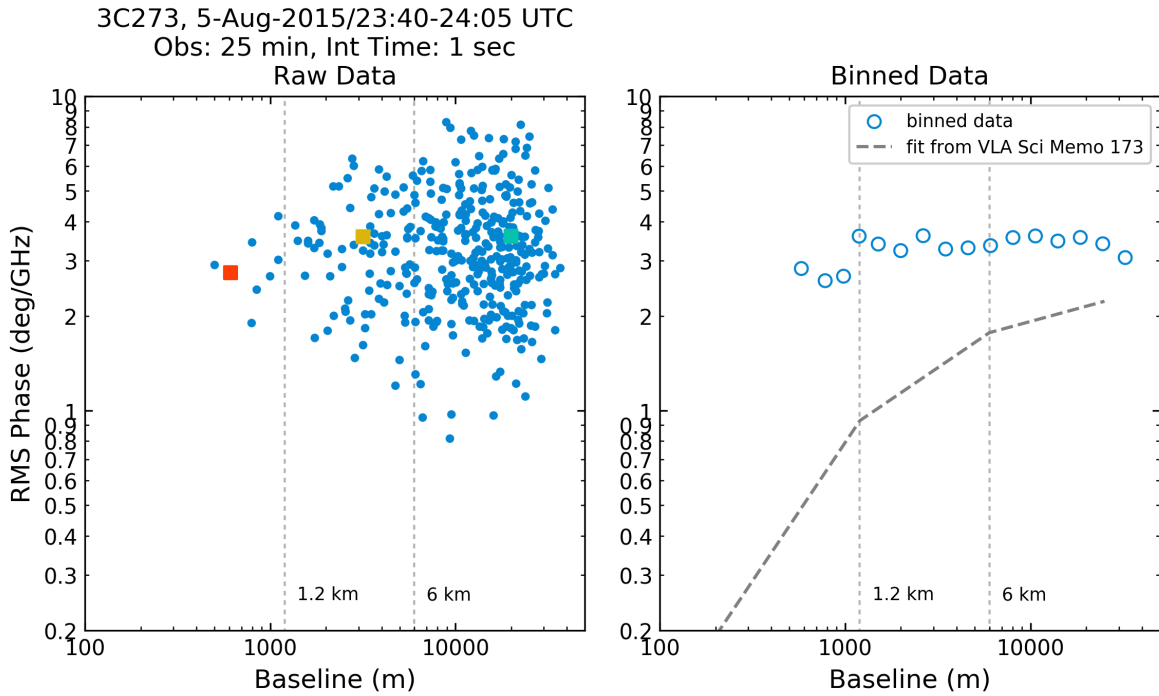
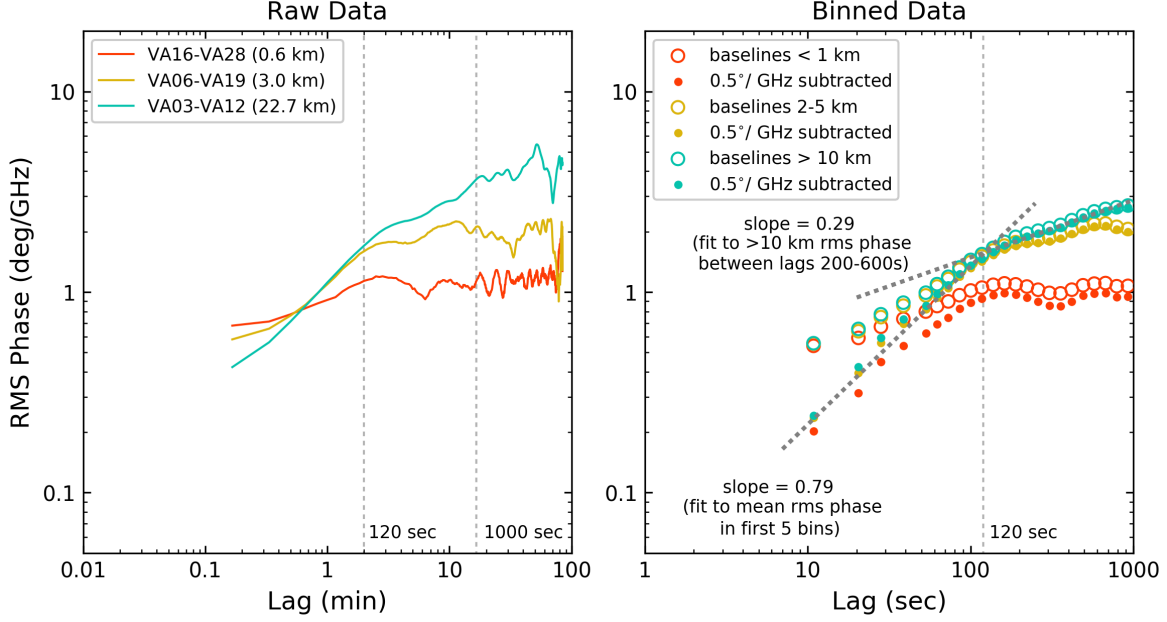


Figure 4 Spatial root phase structure function from a 25 min observation of 3C273 with the EVLA in A configuration starting at 5:40 pm local time on August 5, 2015. The left panel displays rms phase variations versus baseline length for all baselines. The right panel shows binned values. The fit in the right panel is from Carilli & Holdaway (1997) with boundaries indicating the transitions between 3D, 2D, and the outer scale of turbulence.

0748+240, 29-Jan-1997/04:43-06:07 UTC
 Obs: 84 min, Int Time: 10 sec



0748+240, 29-Jan-1997/04:43-05:08 UTC
 Obs: 25 min, Int Time: 10 sec

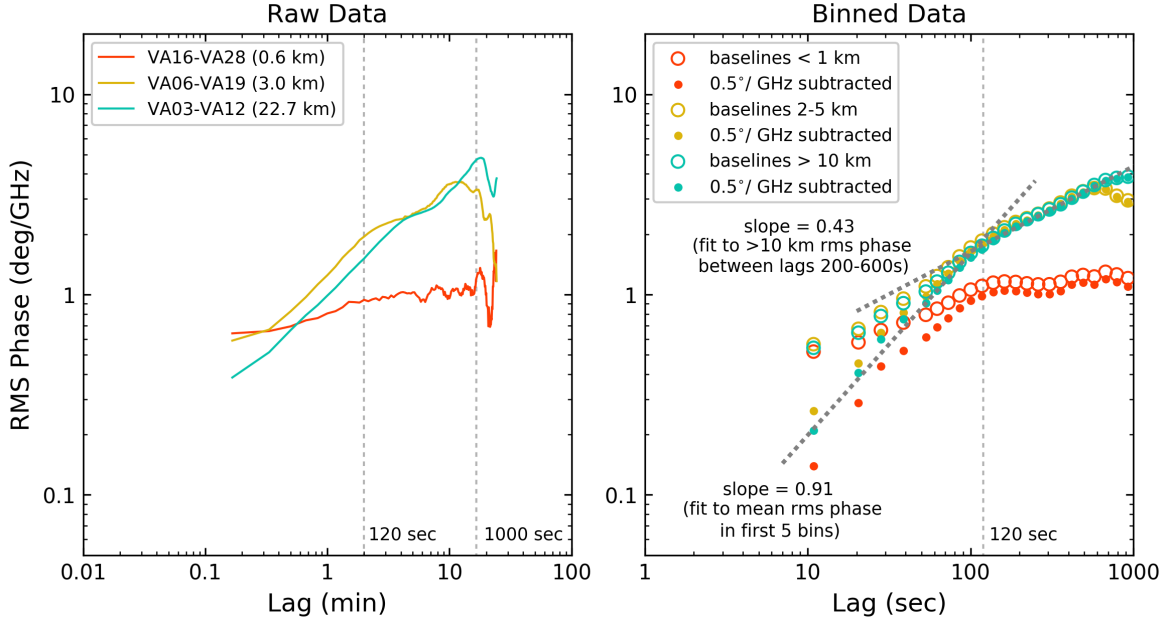


Figure 5 *Upper panels:* Temporal root phase structure function from an 84 min observation of 0748+240 with the VLA in BnA configuration starting at 9:43 pm local time on January 29, 1997. The left panel displays rms phase variations versus temporal lag for the three representative baselines identified in the left panels of Figures 2 and 3. The right panel shows binned values using all baselines within the length ranges indicated in the legend.
Lower panels: Same as upper panels but calculated using data from only the first 25 min of the full 84 min observation.

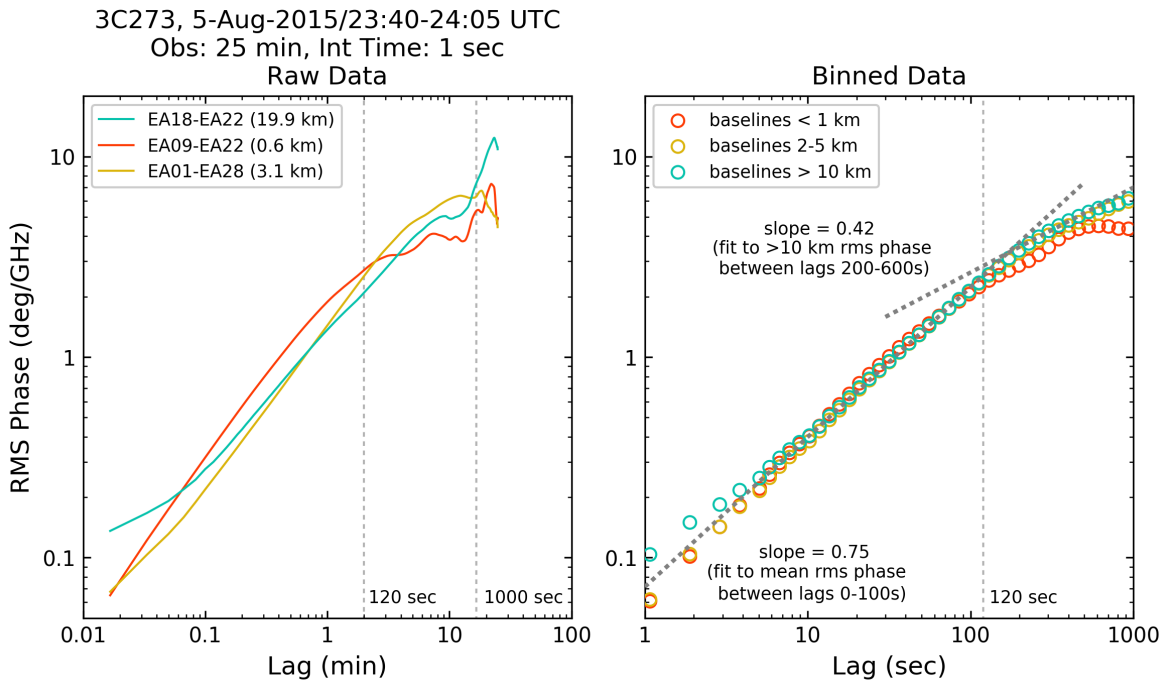


Figure 6 Temporal root phase structure function from a 25 min observation of 3C273 with the EVLA in A configuration starting at 5:40 pm local time on August 5, 2015. The left panel displays rms phase variations versus temporal lag for the three representative baselines identified in the right panel of Figure 2 and the left panel of Figure 4. The right panel shows binned values using all baselines within the length ranges indicated in the legend.